

Wavelet-Based Modelling of Spectral BRDF Data

Luc Claustres, Yannick Boucher, Mathias Paulin

▶ **To cite this version:**

Luc Claustres, Yannick Boucher, Mathias Paulin. Wavelet-Based Modelling of Spectral BRDF Data. Optical Engineering, 2004, 43 (10), pp.2327-2339. 10.1117/1.1789138 . hal-01516275

HAL Id: hal-01516275
https://hal.science/hal-01516275

Submitted on 29 Apr 2017

HAL is a multi-disciplinary open access archive for the deposit and dissemination of scientific research documents, whether they are published or not. The documents may come from teaching and research institutions in France or abroad, or from public or private research centers.

L'archive ouverte pluridisciplinaire **HAL**, est destinée au dépôt et à la diffusion de documents scientifiques de niveau recherche, publiés ou non, émanant des établissements d'enseignement et de recherche français ou étrangers, des laboratoires publics ou privés.

Wavelet-Based Modelling of Spectral BRDF Data

L. Claustres, Y. Boucher, and M. Paulin

Luc Claustres has completed his Ph.D. at the Institut de Recherche en Informatique de Toulouse (IRIT), Université Paul Sabatier (UPS), 118 Route de Narbonne, 31062 Toulouse Cedex 4, France.

E-mail: Luc.Claustres@irit.fr

Tel: +33 (0)5 61 55 83 29

Fax: +33 (0)5 61 55 62 58

Yannick Boucher is a Research Engineer at the Département d'Optique Théorique et Appliquée (DOTA), Office National d'Etudes et de Recherches Aérospatiales (ONERA), BP 4025, 2 Avenue Edouard Belin, 31055 Toulouse Cedex 4, France.

E-mail: Yannick.Boucher@onecert.fr

Tel: +33 (0)5 62 25 26 26

Fax: +33 (0)5 62 25 25 88

Mathias Paulin is an Associate Professor at the UPS, and Researcher at the IRIT.

E-mail: Mathias.Paulin@irit.fr

Abstract

The Bidirectional Reflectance Distribution Function (BRDF) is an important surface property, and is commonly used to describe reflected light patterns. However, the BRDF is a complex function since it has four angular degrees of freedom and also depends on the wavelength. The direct use of BRDF data set may be inefficient for scene modelling algorithms for example. Thus, models provide compression and additional functionalities like interpolation. One common way consists in fitting an analytical model to the measurements data set using an optimization technique. But this approach is usually restricted to a specific class of surfaces, to a limited angular or spectral range, and the modelling quality may strongly depends on the optimization algorithm chosen. Moreover, analytical models are unable to actually handle the BRDF dependence on wavelength.

In this paper we present a new numerical model for acquired spectral BRDF to overcome these drawbacks. This model is based on a separation between the spectral and the geometrical aspect of BRDF, each of them projected into the appropriate wavelet space. After a brief introduction to BRDF, advantages of wavelets and the construction of the model are explained. Then, the performances of modelling are presented and discussed for a large collection of measured and synthetic BRDF data sets. At last, the robustness of the model is tested with synthetic noisy BRDF data.

1 Introduction

The Bidirectional Reflectance Distribution Function (BRDF) characterises the light reflection on surfaces, and is thus used in several domains like scene modelling, image synthesis, optical scattering or remote sensing. The BRDF depends

on five parameters at least: two angles for the incident light direction, two angles for the output direction, and the wavelength. As a consequence, spectral and directional data sets are usually huge, which leads to an unwieldy storage problem. Moreover measurement data sets do not allow a continuous representation of the reflectance. These drawbacks are avoided by modelling. Considerable attention has been given in recent years to the elaboration of BRDF models and also to their classification [1] [2]. Two modelling strategies are widely used:

- explicit models that need an explicit description of the surface in term of simple elements or structures,
- implicit models that do not require an explicit description of the surface but are based on phenomenological approaches or representations of the measurements.

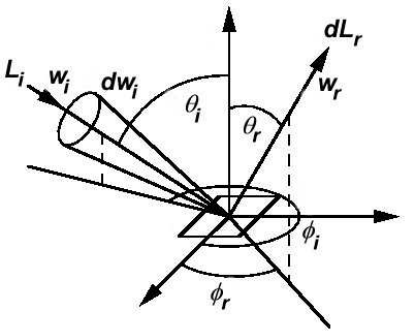
The new wavelet-based numerical model presented in this paper belongs to this last category. It has been designed to efficiently represent, in term of compression and computing time, the spectral BRDF data of all kind of surfaces as long as a measured data set is available.

Section 2 introduces the definition of the BRDF and its properties, then explains the main shortcomings to analytical modelling and particularly to the *measure-and-fit* approach. Section 3 presents the general formulation of the wavelet transform, and its most useful properties. Section 4 describes previous approaches to numerical BRDF modelling using wavelets and the method used to construct our new BRDF model is developed. Section 5 discusses modelling results achieved on real acquired BRDFs as well as synthetic BRDF data set. Section 6 addresses the model sensitivity to multiplicative and additive noise with realistic noise levels. We conclude and point out lines of future research in Section 7.

2 BRDF definition and properties

2.1 Definition

The Bidirectional Reflectance Distribution Function (BRDF) is a distribution in the mathematical point of view, which describes the relationship between the incoming irradiance and the radiance reflected or scattered by a surface. Usually, the BRDF expression is relative to the target's local space [3]:



$$f_r(\omega_i, \omega_r, \lambda) = \frac{dL_r(\omega_r, \lambda)}{dE_i(\omega_i, \lambda)} = \frac{dL_r(\omega_r, \lambda)}{L_i(\omega_i, \lambda)\cos\theta_i d\omega_i}, \quad (1)$$

where E_i is the incoming irradiance, and L_i (respectively L_r) is the incoming (respectively outgoing) radiance in lighting direction $\omega_i = (\theta_i, \phi_i)$ (respectively viewing direction $\omega_r = (\theta_r, \phi_r)$). This definition ignores polarization, time variation, frequency shift, and surface position dependence in order to reduce complexity. This BRDF definition is accurate enough for most remote sensing applications and scene modelling purposes. BRDF support is then reduced to $\mathcal{H}_i^2 \times \mathcal{H}_r^2 \times \mathcal{R}$ where $\mathcal{H}_i^2$ is the incident hemisphere, $\mathcal{H}_r^2$ is the reflection hemisphere, and $\mathcal{R}$ the wavelength space.

2.2 Physical Properties

The BRDF has four important and interesting properties:

1. *Non-negativity*: BRDF value is strictly positive

$$f_r(\theta_i, \phi_i, \theta_r, \phi_r, \lambda) \geq 0 \quad (2)$$

2. *Helmholtz reciprocity*: the behavior of the surface is independent of the luminous flux direction [4] , i.e.

$$f_r(\theta_i, \phi_i, \theta_r, \phi_r, \lambda) = f_r(\theta_r, \phi_r, \theta_i, \phi_i, \lambda) \tag{3}$$

3. *Energy conservation*: the energy reflected by the surface is not greater than the incoming energy on the surface, i.e. for each possible incoming direction ω_i and outgoing direction ω_r (assuming integration over wavelength is implied)

$$\frac{d\Phi_r}{d\Phi_i} = \frac{\int\limits_{\mathcal{H}_i^2}\int\limits_{\mathcal{H}_r^2} f_r(\omega_i, \omega_r) L_i(\omega_i) \cos\theta_i \cos\theta_r d\omega_i d\omega_r}{\int\limits_{\mathcal{H}_i^2} L_i(\omega_i) \cos\theta_i d\omega_i} <= 1, \tag{4}$$

where $d\Phi_i$ (respectively $d\Phi_r$) is the incoming (respectively outgoing) luminous flux

4. *Isotropy*: for a lot of surfaces the reflectance does not change with respect to the surface orientation (*isotropic* BRDF), i.e. for any wavelength

$$f_r(\theta_i, \phi_i, \theta_r, \phi_r) = f_r(\theta_i, 0, \theta_r, |\phi_r - \phi_i|) = f_r(\theta_i, \theta_r, \phi = |\phi_r - \phi_i|) \tag{5}$$

otherwise the BRDF is said to be *anisotropic*.

For measurements on homogeneous surfaces, Equation (3) allows to simplify BRDF data sets [5]. This simplification is often used in image synthesis. However for real measurements on heterogeneous surfaces, this equation is not strictly applicable.

2.3 Modelling BRDF

BRDF is an input data of several applications including target and background signature modelling, radiative transfer simulation, and inversion of thematic physical

models. However, the large amount of measurement samples needed to accurately describe the BRDF does not allow the use of raw data, and modelling is usually required. Indeed lots of applications, like scene modelling, manage many different BRDFs at the same time and memory requirement can be easily prohibitive. On the one hand a model has to provide a good compression scheme. On the other hand we are interested in a convenient, accurate, and efficient representation. These reasons mainly explain the success of analytical models, but these models are not well-suited for spectral BRDF modelling of arbitrary surfaces.

Actually, model parameters for most surfaces are not directly available. Advanced numerical optimization techniques retrieve the best parameter values by minimizing a distance between modelled and measured data. This modelling can suffer from numerical instabilities in non-linear fitting routines, and results strongly depend on initial conditions. Secondly, analytical models, either phenomenological or based on a physical theory, lack generality. Physically-based models start with specific assumptions about the surface and are only able to predict the reflectance of surfaces that closely match those assumptions. Phenomenological models are custom-made and are not suitable for arbitrary BRDF. Moreover, as the viewing angle of the sensor increases, the effects of BRDF become exacerbated, and significantly affect the accuracy in off-nadir views. Thus, most analytical models become not appropriate in these cases. Therefore, models should cover the entire range of possible angles of incidence and reflection. At last, to the best of our knowledge, no analytical model explicitly handles the wavelength dependence of the BRDF.

These reasons press us to develop a new numerical BRDF model, more general as it does not rely on either specific assumptions or physical theory. The

main idea is to project the BRDF measurement data set onto a new space, which is usually more efficient and convenient. Primer representations based on projective methods for BRDF modelling used *spherical harmonics* [6] [7] [8]. But the evaluation cost of these functions is prohibitive due to their *global support* on the sphere. Wavelets are *locally defined*, consequently they are faster. Furthermore they offer a better and more flexible compression scheme. There are also some mathematical constructions of wavelets based on spherical harmonics [9] [10] but they have no concrete application and are still at a formal state.

3 Wavelet theory

3.1 Introduction

Wavelets have become very popular during the last decade due to many of their interesting properties [11] [12]:

- *compression*: able to manage large data sets
- *multiresolution*: a reconstruction at different levels of accuracy is possible
- *efficiency*: the reconstruction of the signal is done in a logarithmic time according to the number of samples
- *denoising*: small and localized signal variations are avoided by the compression

Moreover wavelets handle low-frequency signals with localized high-frequencies very well. They should be naturally adapted to the strong variations of acquired BRDFs (specular peak, hot-spot phenomenon).

3.2 Definition

The discrete wavelet transform is a filtering operation that separates a signal into a low-frequency part (*approximation*) and a high-frequency part (*details*), via *convolution* (projection on a wavelet function basis). Then separating again, recursively, the approximation part, the discrete wavelet transform leads to a decomposition at different *resolutions* or *scales*. The more general formulation of the discrete wavelet transform of a sampled function f can be written as follows:

$$f = \sum_k a_0^k \varphi_0^k + \sum_{j=0}^{n} \sum_m d_j^m \psi_j^m \tag{6}$$

ψ_j^m (respectively φ_j^k) is the wavelet (respectively scaling) function number m (respectively k) at decomposition level number j. The first one encodes the details while the second one encodes the approximation of the sampled function f. The corresponding projection coefficients d_j^m and a_j^k are computed using fast recursive algorithms. Computing scaling and wavelet coefficients from a fine resolution to a coarser resolution is called *analysis*:

$$a_j^k = \sum_l \tilde{h}_j^{k,l} a_{j+1}^l \tag{7}$$

$$d_j^m = \sum_l \tilde{g}_j^{m,l} a_{j+1}^l \tag{8}$$

The inverse operation, consisting in retrieving the finest approximation starting from coarser level, is called *synthesis*:

$$a_{j+1}^l = \sum_k h_j^{k,l} a_j^k + \sum_m g_j^{m,l} d_j^m \tag{9}$$

Wavelet transform may be viewed as a filtering operation where coefficients $\tilde{h}, \tilde{g}$ are analysis filters and h, g are synthesis filters. Wavelet compression consists in removing weak wavelet coefficients (setting their values to zero) in the final decomposition of the function (equation 6). The analysis process computes the final

decomposition of the function (wavelet transform) while the synthesis process reconstructs the function from its compressed version (inverse wavelet transform). The main thing to notice is that this formulation is *generic* because it does not rely on a particular wavelet function or support space. As a consequence, algorithms are pretty similar for any transform. There is only one requirement: the support space must be a *Hilbert* space [13].

4 Wavelet-based BRDF modelling

4.1 Introduction

A parallel can be drawn between the analytical approach [14] and a numerical approach based on wavelets. Indeed, the spirit of both methods is very similar and both modelling process are illustrated on Figure 1. The *inverse mode* consists in retrieving the model's parameters from the measurement data set. In the analytical case a numerical optimization is performed while in the numerical case wavelet transform and compression are applied. The *direct mode* consists in computing the BRDF value for any possible incoming/outgoing direction and wavelength, from the model's parameters. In the analytical case the model formula is evaluated while in the numerical case the inverse wavelet transform and an interpolation scheme are applied. The better the model is, the lower the distance between the original and the simulated BRDF is. Before the complete presentation of the modelling process in the next sections, we present previous work on wavelet-based BRDF modelling.

4.2 Previous work

Schröder et al. [15] are the first researchers to mention the use of wavelets for BRDF modelling. They introduce *spherical wavelets* to efficiently represent functions on the sphere $\mathcal{S}^2$. A function defined over $\mathcal{S}^2$ is approximated by a piecewise constant function over a set of triangles almost regular in term of solid angle [1]. The triangle set is constructed using a recursive subdivision starting from an octahedron (or a tetrahedron on the hemisphere $\mathcal{H}^2$). At each level the triangles are subdivided into four children, then projected on the sphere, until a given *accuracy level* (Figure 2).

Schröder et al. define a multiresolution analysis in the space of finite energy functions defined over $\mathcal{S}^2$ thanks to the *lifting cheme* [16]. The spherical wavelet basis (Figure 3) is a Haar-like basis derived from the well-known Haar basis [17] [18]. The most important thing to notice is that this construction is *parameterization independent*, which is not the case of a previous method introduced by [19] using tensor product. But the work of Schröder et al. is still restricted to function defined over $\mathcal{H}^2$ while BRDF is potentially a 5D function defined over $\mathcal{H}^2 \times \mathcal{H}^2 \times \mathcal{R}$ (incident and outgoing direction, and wavelength). In fact, spherical wavelets are suitable for directional-hemispherical reflectance, or BRDF at a fixed incident direction, without taking into account the dependence on wavelength.

A more complete model was presented by Lalonde et al. [20]. They use multidimensional wavelets (4D) on the real line to handle BRDF at fixed wavelength, which requires a mapping from $\mathcal{H}^2 \times \mathcal{H}^2$ to $\mathcal{R}^4$. The use of *Nusselt* embedding [21], to compromise on the matter of redundancy at the poles, provides an elegant solution but cannot entirely avoid the distortion introduced by the map-

[1] Generating a uniform distribution of points on the sphere is still an open problem

ping. This representation is still strongly *parameterization dependent*. The global control of the compression (*thresholding*) induced by the single multidimensional wavelet transform is also one of the most important drawbacks of this representation. Nevertheless, this work should be easily extended to include the dependence on wavelength (with an additional dimension).

4.3 Model description

In this section we introduce a new BRDF model based on wavelets. Our contribution is to separate the BRDF into a spectral part defined over $\mathcal{R}$ and a directional or geometrical part defined over $\mathcal{H}^2$. Each part is projected *independently* on the appropriate wavelet space, that is using spherical wavelets for the angular dependence, and one-dimensional wavelets for the dependence on wavelength. We have chosen the *standard* approach [11] that uses product of decompositions to transform multidimensional signals, in contrast with the *non-standard* approach [11] (used by Lalonde), which consists in building multidimensional wavelet bases from one-dimensional bases using a tensor product of basis functions. The key idea is to perform multiple *atomic* transforms, that is to say transforms defined over a single space (not a product of spaces), instead of using a single multidimensional transform. The last method is theoretically more efficient, but the former has many advantages.

First we can increase the compression ability by exploiting the coherence in each space in addition to the coherence in the hidden dimension-connections. Secondly a *partial* transform or reconstruction can be computed, i.e. we do not need to perform the complete 5D transform. Indeed, we can choose which spaces will be used, providing a more flexible model that allows the representation of all kind

of BRDF: isotropic, anisotropic, spectral or at a fixed wavelength. At last, our approach does not require any mapping since the model is naturally defined on the support of the BRDF.

4.3.1 BRDF projection

The initial step of our method consists in projecting the BRDF measurement data set into the appropriate wavelet spaces. A first recursive subdivision is used to store BRDF data according to the incoming direction. Each triangle of the subdivision stores the directional-hemispherical reflectance distribution corresponding to the direction aimed by the triangle centre. Then, a second recursive subdivision is used to store the reflectance data according to the outgoing direction. Each triangle stores a real value, or a spectrum in the spectral case. Two spherical wavelet transforms are applied in the case of a BRDF at a fixed wavelength (on incoming and outgoing directions). In the case of a spectral BRDF, an additional level is required: a one-dimensional wavelet transform is applied on each BRDF spectrum.

Although only one wavelet basis is available for the spherical transform, many bases are available for the dependence on wavelength since one-dimensional bases are common [11]. Our model selects the best basis according to the modelling error among a set of 52 different bases. Nevertheless, many bases belong to the same family but differ from one another in their properties (vanishing moments, support width, order, etc.): Daubechies [22], Symmlet [11], Coiflet [23], Battle-Lemarié [24], Beylkin [23], Adelson [25], FBI [26], Vaidyanathan [27] Antonini [28], Villasenor [29] [30] [31], Burt-Adelson [11], Brislawn [32], Cohen-Daubechies-Feauveau (CDF) [33], Spline [11], Odegard [34], and Pseudo-Coiflet

[35]. The restriction to the use of the Haar basis on the recursive subdivision is not annoying because this basis is well-suited to signals with discontinuities as shown by Schröder [15]. It will be efficient for BRDF modelling of shiny surfaces with narrow peaks, which are very common in scene representing artificial surfaces. Moreover, it allows a fast sampling scheme based on the multiresolution of the wavelet decomposition to perform importance sampling of the BRDF. This technique can dramatically reduce the variance of Monte Carlo simulations [36] intensively used into radiative transfer codes.

In fact, isotropic BRDFs are simpler than anisotropic ones, and this property can be used to simplify the transform process. Indeed, any BRDF value can be recovered from the BRDF data in the plane where $\phi_i = 0$, by a rotation of ϕ around the local surface normal. So the spherical wavelet transform on incoming directions is not relevant here, since we do not store all BRDF measurements but only a small part according to the plane where $\phi_i = 0$. Avoiding this transform is possible without any fuss using the standard approach, while it is not possible with the non-standard approach, which would require the elaboration of a specific 3D model instead of the general 5D model. With our approach, we simply have to ignore the atomic wavelet transform on $\mathcal{H}_i^2$ and to perform both other atomic transforms on $\mathcal{H}_r^2$ and $\mathcal{R}$.

The technical details of the model, as well as the algorithms and the data structures needed for implementation can be found in [36]. We have put the source code for a wavelet-based representation of different radiometric terms into a C++ library called *The Discrete Wavelet Transform Library* (DWTL). The DWTL is part of the *Ray Of Light* project, and is available for free at http://www.realistic-rendering.org.

4.3.2 Compression strategy

Wavelet coefficients express local signal coherence at different levels according to a specific norm. If a coefficient is weak, there will be no strong variation between two levels, so the lowest level will approximate information without introducing a large error. Thus, wavelet compression is simply done by removing weak coefficients of the projected BRDF.

In our modelling approach, the wavelet compression is performed in each space where the transform took place. The coherence between directional-hemispherical reflectances according to incoming direction is fully used. The same for spectra coherence and for BRDF values according to reflected direction. At last, the coherence according to wavelength for spectral BRDFs is also used. We have demonstrated in [36] that for a given error level we can reach a better compression ratio than obtained by Lalonde.

Usually, multidimensional wavelet transform uses a single threshold, which implies a global error control. We have prefered to use a global threshold for *each* space. Furthermore, we have set up an adaptive threshold, starting from each global threshold, by scaling the threshold according to the local level of the BRDF.

4.3.3 BRDF reconstruction

The inverse wavelet transform only allows the reconstruction of the original discrete BRDF, starting from the compressed version. But many applications, such as radiative transfer codes, require a BRDF continuously defined for all combinations of incident angles, reflected angles, and wavelengths. Consequently, we have interpolated the BRDF values after the reconstruction. A detailed study of interpolation techniques is out of the scope of this paper, and is not related to the

wavelet representation. Indeed, the estimation of a function f for arbitrary configurations, where only a sampled version of f is available, is a central problem in signal processing [37].

Here we use well-known interpolation methods depending on the requirements: for C^0 BRDF, we use linear interpolation for the spectral part and barycentric interpolation over the triangles [38] for the directional one; for a more continuous BRDF (C^2), we use cubic B-Splines [37] for the spectral part and Clough-Tocher interpolant [39] for the directional one.

5 Results

For determining the performances of the model, we need estimators of the difference between the original BRDF and the simulated one after an analysis-synthesis cycle. Particularly, we have chosen the relative errors ϵ_1^r and ϵ_2^r in term of $\mathcal{L}_1$ and $\mathcal{L}_2$ norms according to compression ratio:

$$\epsilon_1^r = \frac{1}{n}\sum_i \frac{|f_i' - f_i|}{f_i} \tag{10}$$

$$\epsilon_2^r = \sqrt{\frac{1}{n}\sum_i \frac{(f_i' - f_i)^2}{f_i^2}} \tag{11}$$

where f_i are the values of the original BRDF, f_i' are the values of the reconstructed BRDF from its compressed version, and n is the total number of samples in the measurement data set. The compression ratio r_c is the ratio of the initial number of measurement points to the final number of remaining wavelet coefficients after compression. It is related to the compression rate t_c (percentage of initial data removed by compression) by the following expression:

$$t_c = 100 - (\frac{100}{r_c})$$

The number of wavelet coefficients for a compression ratio of 1:1 is equal to the initial number of samples for the measured BRDF, i.e. the BRDF is just projected into the wavelet spaces without any compression. A small initial error appears for this projection because $\mathcal{S}^2$ is sampled regularly in term of (θ, ϕ) angles for the BRDF measurement and not regularly in term of solid angle as the recursive subdivision does.

5.1 Data

In this paper we present results achieved on measured and simulated BRDFs. Real BRDFs have been measured by the goniometer set up at the ONERA [40], over a wide variety of surfaces. We have selected artificial targets (cloth, plastic, plywood, spectralon, velvet), but also natural ones (green and dry grass, wood, sand). The total number of measurement points is 485,376 for one material (476 directions and 1024 wavelengths). The precision of the measurement is better than 5% in the spectral range 420-950 nm with a spectral resolution of 3 nm and a spectral sampling of 0.5 nm. However, we have used here a spectral sampling step of 5 nanometers, which is fine enough for our requirements. Zenithal angles are sampled every ten degrees, and the relative azimuth angle every twenty degrees.

5.2 Estimation of the modelling error

5.2.1 Reflectance spectra

Because our BRDF representation has two independent parts, one for the directional aspect of the data, and one for the spectral aspect of the data, these two parts can be used as stand-alone representations.

For this reason, we have first tested the spectrum modelling with reflectance spectra extracted from measured BRDFs at fixed incoming and outgoing direction, but also with other radiometric terms such as spectral measured radiance and emissivity. The Figure 4 shows the compression rate achieved according to different wavelet bases, for a constant modelling error $\epsilon_2^r = 2$ %, and on different acquired spectra. A graphical representation of the reconstructed spectra is shown in Figures 5 and 6, corresponding respectively to the spectral emissivity of a paint, and the spectral radiance of sand, with different compression ratios.

Table 1 contains more quantitative results and shows that our model is efficient to represent many different kind of spectrum with a small number of samples from the initial data. In this table, r1 (respectively r2) is a green grass (respectively paint) reflectance measured in the spectral range 0.3-4 microns; l1 (respectively l2) is a sand (respectively canopy) radiance measured in the spectral range 0.3-13.6 microns; e1 and e2 are IR paint emissivities measured in the spectral range 2.5-21 microns. Moreover, the model provides a smooth profile for the spectrum by removing the noise. Even if the modelling error growths with the compression ratio, we think that, in many cases, a better spectral profile is reconstructed, because of the denoising. This interesting property will be investigated precisely in Section 5.3.

5.2.2 Isotropic BRDF

BRDF for fixed wavelengths : Table 2 presents compression ratios and corresponding modelling errors for acquired isotropic BRDFs at different fixed wavelengths. All measurement data sets can be compressed up to 64:1 with a global $\mathcal{L}_1$ and $\mathcal{L}_2$ error<10%, except the plastic one. This sample is the most specular (dif-

fuse and specular parts differ by a factor 100), with a large peak leading to a large discontinuity. As the wavelet transform is basically a filtering operation, a high compression ratio smooths the specular peak. However, the specular peak is well-preserved with a medium compression rate. Moreover, we have shown in [41] that wavelet modelling has similar performances than the analytical modelling at fixed wavelength for diffuse surfaces, and better ones for specular surfaces.

Figure 7 shows the plots of the BRDF of three different samples (cloth, sand, and dry grass) for a fixed incoming direction and azimuth angle. The worst results, apart from the plastic one, are achieved for the dry grass (Table 2), which is the measurement with the lowest BRDF level (about 0.03 sr^{-1}). Thus, for a constant noise level, the signal-to-noise ratio (SNR) is weaker and the signal is lower. In this case the model hardly makes the difference between BRDF variations and noise (Figure 7c). In contrast, modelling is accurate for the sand and the cloth sample, even for some radical thresholds. The wavelet-based representation correctly handles the backscattering of the sand sample (Figure 7b) and the relative "specularity" of the cloth sample (Figure 7a).

Spectral BRDF : Table 3 shows results achieved on isotropic spectral BRDF data. For each compression ratio, the best wavelet basis selected by the model is given. Modelling error according to compression is often better than it is in the case of a fixed wavelength (especially for the plastic BRDF). All available measurement data sets can be compressed up to 128:1 and a global $\mathcal{L}_1$ error<10% and $\mathcal{L}_2$ error<20%. The main reason is the smooth spectral variations of the BRDFs. The behaviour of the model is compared to the measurements, as illustrated in Figure 8 for the cloth target and two different wavelet bases and compression ratios. In addition to the modelling error, the spectral shape might be a criterion for

the wavelet basis selection. Indeed, this shape strongly depends on properties of the chosen basis.

However few materials present larger errors than those obtained in the case of fixed wavelength. One possible explanation is influence of the noise, which is not spectrally flat. Actually, our data are especially noisy in the range 400-450 nm and the compression removes this noise, that introduces an error with no physical signification (Figure 9), which only represents the difference between the original noisy spectrum and the simulated denoised one.

5.2.3 Anisotropic BRDF

The goniometer of the ONERA is fully automatic for isotropic measurement, but for anisotropic measurement, a manual rotation is applied to the sample between each acquisition, resulting in an unwieldy process. This is the reason why we have measured a single anisotropic material (a glazed velvet), with an azimuth angle step of fifteen degrees. The final number of samples was 6,309,888 for the whole BRDF data set. The velvet sample presents pronounced directional effects (anisotropy), and the detection limit of the device is reached in some part of the measured BRDF. In those parts, the overall signal level is very low and the (SNR) is very weak. To be more exhaustive in the fixed wavelength case, we have also tested the performances of the model with synthetic BRDF data sets.

BRDF for fixed wavelengths : Table 4a presents the modelling error for the anisotropic velvet BRDF data set and for a synthetic BRDF data set generated using the anisotropic Ward's BRDF model [42]. Until a compression ratio of 16:1, modelling is as good for the velvet as for the synthetic data. Beyond this ratio, the $\mathcal{L}_2$ error becomes very large for the velvet sample unlike for the synthetic

BRDF, while the $\mathcal{L}_1$ error is still good in both cases. This phenomenon is here again probably induced by the noise of the measurements on the velvet. Indeed, relative $\mathcal{L}_2$ error is more sensitive to modelling errors for low BRDF levels. As wavelet compression smoothes the BRDF and removes the noise, the modelling error always raises with the compression ratio, even if denoising is, in some cases, an interesting property of the model.

Spectral BRDF : In the spectral case, as far as we know, no analytical BRDF models are available, so the performances of the model have only been estimated with the glazed velvet data set. As expected, we have noticed the same increase of the $\mathcal{L}_2$ error with compression ratio, but more strongly marked (see Table 4b). The most probable reason is that the SNR of the measurement device depends on the wavelength and is relatively weak in some regions of the spectrum. Indeed, some measured BRDF values in the range 400-450nm are negative because of the noise, that has no physical meaning. To ensure the non-negativity rule (Equation 2), we have replaced these negative values by a low BRDF bound. This process introduces yet virtual discontinuities in the smooth BRDF spectra with, as a consequence, oscillations around the discontinuities after compression (Figure 10). This effect, known as the Gibbs Phenomenon [43], may explain, at least partly, the large $\mathcal{L}_2$ observed error.

5.3 Noise sensitivity

Robustness is one of the most important properties desirable for modelling of measurement data set. In particular, measured BRDF data are always more or less noisy, and the model should be proof against measurement noise. In this

Section we estimate the sensitivity of our model according to Gaussian additive and multiplicative noises.

5.3.1 Data

First of all, a BRDF data set had to be chosen for this study. Since measurements are noisy by nature, we have used a synthetic data set to test the robustness of the model, so as to be able to parameter the noise level. We have built a virtual measurement data set using the Phong's BRDF model [44], which calculates the directional variations of the synthetic BRDF. At this first directional kernel, we have added a spectraly-dependent kernel. Its spectral profile $S(\lambda)$ is a unit frequency-varying sine curve with an amplitude of ± 20 %, with no physical realism but that allows us to test the performance from smooth to strong spectral variations between 0.5 and 1 micron:

$$S(\lambda) = 1 + 0.2 * \cos(2 * \pi * \lambda/\lambda_0) \text{ with } \lambda_0 = -150/500 * \lambda + 350\text{nm},$$

where λ belongs to the range $[500\text{nm}, 1000\text{nm}]$. For each possible directions set, the spectrum is scaled by the BRDF level computed through the evaluation of the Phong's model, and modulated by $S(\lambda)$. Spectral sampling is done every 2 nanometer and the recursive subdivision level for the spherical wavelet projection is equal to 3, which results in a set of 449,792 samples.

Secondly, we have taken care to set realistic noise levels for this experiment. For convenience, we have not considered the spectral variation of the noise. The additive noise level has been estimated from a simple dark measurement on a perfect absorber. This level is about $10^{-3} sr^{-1}$ at nadir viewing for the considered measurement device. A realistic additive noise follows a law in $1/\cos\theta_r$ [45], and we have also taken this effect into account to closely match the device noise.

Multiplicative noise level can be estimated from the standard deviation of real and spectraly flat measured BRDFs. For our device, this level is about 0.2 %, and does not depend on angular variations. To perform a more complete evaluation, we have not limited ourselves to these levels and have also included several higher noise levels.

5.3.2 Method

We have constructed two initial data sets for this test. The first one was the compressed version of the synthetic BRDF, using a Villasenor wavelet basis and a compression ratio of 8:1 (case I). The second one was using a Brislawn wavelet basis and a compression ratio of 16:1 (case II). The modelling error introduced by the compression is presented in Table 5.

The method consists in adding noise to the initial BRDF data sets according to a chosen noise type and level. A first comparison is performed, called "initial case", to evaluate the impact of the noise without any compression. Then, the noisy data set is compressed with the same configuration used for cases I and II. The final step for the completion of the test consists in comparing the simulated sets to the original one as illustrated in Figure 11.

For a more qualitative evaluation, we also include *spectral angle* comparisons. The spectral angle is a physically-based spectral criterion that supplies the spectral similarity between two spectra by calculating the angle between them, treating them as vectors in a space with dimensionality equal to the number of bands [46]. Usually, a spectral angle < 0.1 radian means that spectra are very similar. We choose three different spectral angles as_1, as_2, and as_3, corresponding respectively to the following configurations: $[\theta_{i_1} = \theta_{r_1} = 60, \phi_1 = 180]$,

$[\theta_{i_2} = \theta_{r_2} = 60, \phi_2 = 0]$, and $[\theta_{i_3} = 60, \theta_{r_3} = 30, \phi_3 = 180]$.

5.3.3 Results for multiplicative noise

Table 6 summarizes the results achieved on noisy data in the multiplicative case. One can see that the model is able to remove low noise level with the highest compression ratio (case IIa and IIb). The modelling error is quite similar to the one obtained for compressed noise-free data (initial cases I and II). On the other hand, the lowest compression ratio is not sufficient to denoise the data. Nevertheless, compression always provides a beneficial effect on the noisy spectrum, since the shape of the spectrum after compression is closer to the original noise-free spectrum, as shown by the different values of the spectral angle. Moreover, for the highest noise level, the modelling error induced by the noise is larger than the one induced by the compression. This error is reduced by a large amount as the compression ratio increases.

Figure 12 shows a close-up for a multiplicative noise of 5% (case IIc) in the range 500-600 nm. One can see that the model is not sensitive to the noise, because the compressed noise-free BRDF spectrum closely match the compressed noisy BRDF spectrum. The small offset between these two spectra is due to the compression in the geometrical domain (spherical wavelet transform) that generates a spectral approximation in the neighbourhood of a given direction by averaging spectra around.

Figure 13 represents the four BRDF sets (noise-free uncompressed, noise-free compressed, noisy uncompressed, and noisy compressed) at fixed wavelength and fixed incoming direction. Here again, the compressed noisy set is closer to the original set than the uncompressed noisy set.

5.3.4 Results for additive noise

Table 6 contains the results achieved on noisy data in the additive case. The noise increases with the reflection angle θ_r with respect to the law in $1/\cos\theta_r$. At grazing angles, the high noise level explains that the difference between the compressed noisy set and the original one is larger than in the multiplicative case. However, the model presents the same overall behaviour: compression always improves the similarity between compressed noisy and noise free data sets, as shown by the spectral angles values, even at grazing angles.

Figure 13 represents the four BRDF sets (noise-free uncompressed, noise-free compressed, noisy uncompressed, and noisy compressed) for an additive noise level of $5 * 10^{-3} sr^{-1}$ (case If) at fixed incoming and outgoing directions in the range 800-900 nm. The compressed noisy BRDF set is very similar to the compressed noise-free BRDF set. Moreover, variations due to the noise cannot be confused with the spectral BRDF variations.

6 Conclusion and future work

We have presented a new BRDF model based on wavelets to overcome the main shortcomings to analytical modelling. This model is suitable and efficient for any kind of BRDF measurement data set, without any spectral or angular range limitation. It has been tested against many different surface samples and the model agrees reasonably well with the measurements, even for some radical compression thresholds. Usually, isotropic BRDFs can be compressed up to 64:1 with a global relative error < 10%. The model is less impressive on anisotropic BRDFs, but the main reason is certainly the poorer quality of the measurement in this case.

Indeed, results are still pretty good with a synthetic anisotropic BRDF data set. Moreover we have demonstrated the denoising capability of the model for synthetic BRDF data sets. The model is very robust to moderate but realistic noise levels, for multiplicative noise as well as additive noise, and the compressed noisy BRDF data set is always closer to the original noise-free data set than the uncompressed noisy data set.

Nevertheless, some work remains to be done. Interpolation schemes in the specific case of BRDF should be more deeply investigated. Another perspective is to improve spherical wavelet bases. We should for instance use the work of Bonneau [47] about the design of Haar-like bases thanks to *semi-orthogonality*. In the same way, one-dimensional basis selection should be more efficient using the *best basis* algorithm [48]. At last, we left as future work the use of the wavelet projection for classification, like Kaewpijit did [49] for hyperspectral data.

Acknowledgements

We specially thank Sophie Lacherade, Emmanuel Christophe and Christophe Miesch for their contributions to the final version of this paper.

References

[1] N.S. Goel. Models of vegetation canopy reflectance and their use in estimation of biophysical parameters from reflectance data. In *Remote Sensing Reviews*, volume 4, pages 1–212, 1988.

[2] B. Pinty, N. Gobron, J.-L. Widlowski, S. A. W. Gerstl, M. M. Verstraete, M. Antunes, C. Bacour, F. Gascon, J.-P. Gastellu, N. Goel, S. Jacquemoud, P. North, W. Qin, and R. Thompson. Radiation Transfer Model Intercomparison (RAMI) Exercise. *Journal of Geophysical Research*, 106(D11):11,937–11,956, 2001.

[3] F. E. Nicodemus, J. C. Richmond, J. J. Hsia, I. W. Ginsberg, and T. Limperis. Geometric Considerations and Nomenclature for Reflectance. Monograph 161, National Bureau of Standards (US), October 1977.

[4] M. Minnaert. The Principle of Reciprocity in Lunar Photometry. *Astrophysical Journal*, 93:403–410, 1941.

[5] W.C. Snyder. Reciprocity of the BRDF in Measurements and Models of Structured Surfaces. *IEEE Transactions on Geoscience and Remote Sensing*, 36(2):685–691, 1998.

[6] B. Cabral, N. Max, and R. Springmeyer. Bidirectional Reflection Functions from Surface Bump Maps. In *Computer Graphics (ACM SIGGRAPH '87 Proceedings)*, volume 21, pages 273–281, 1987.

[7] Francois Sillion, James R. Arvo, Stephen H. Westin, and Donald P. Greenberg. A Global Illumination Solution for General Reflectance Distributions.

In *Computer Graphics (ACM SIGGRAPH '91 Proceedings)*, volume 25, pages 187–196, July 1991.

[8] Stephen H. Westin, James R. Arvo, and Kenneth E. Torrance. Predicting Reflectance Functions From Complex Surfaces. In *Computer Graphics (ACM SIGGRAPH '92 Proceedings)*, volume 26, pages 255–264, July 1992.

[9] W. Freeden and U. Windheuser. Spherical Wavelet Transform and its Discretization, Tech. Rep. 125. Technical report, Universität Kaiserslautern Fachbreich Mathematik, Kaiserslautern , Germany, 1994.

[10] M. Conrad and J. Prestin. *Multiresolution on the Sphere*, pages 165–202. Springer-Verlag, Heidelberg, 2001.

[11] I. Daubechies. *Ten Lectures on Wavelets*. Society for Industrial and Applied Mathematics, Philadelphia, 1992.

[12] S. Mallat. *A Wavelet Tour of Signal Processing*. Academic Press, San Diego, 1999.

[13] M. R. Raghuveer and S.B. Ajit. *Wavelet Transforms : Introduction to Theory and Applications*. Addison-Wesley, Reading, 1999.

[14] M. M. Verstraete, B. Pinty, and R. E. Dickinson. A physical model of the bi-directionnal reflectance of vegetation canopies. *Journal of Geophysical Research*, 95(20):755–765, 1990.

[15] Peter Schroder and Wim Sweldens. Spherical Wavelets: Efficiently Representing Functions on the Sphere. In *Computer Graphics Proceedings, Annual Conference Series, 1995 (ACM SIGGRAPH '95 Proceedings)*, pages 161–172, 1995.

[16] Wim Sweldens. The Lifting Scheme: A Construction of Second Generation Wavelets. *SIAM Journal on Mathematical Analysis*, 29(2):511–546, 1998.

[17] M. Girardi and W. Sweldens. A New Class of Unbalanced Haar Wavelets that form an Unconditional Basis for Lp on General Measure Spaces. Technical Report 1995:2, Departement of Mathematics, University of South Carolina, Carolina, May 1995.

[18] M. Mitrea. Singular Integrals, Hardy Spaces and Clifford Wavelets. *Communications of the ACM*, 32(6):343–349, 1980.

[19] S. Dahlke, W. Damen, E. Schmitt, and I. Weinreich. Multiresolution Analysis and Wavelets on S2 and S3, Tech. Rep. 104. Technical report, Institut fur Geometrie und Angewandete Mathematik, Aachen , Germany, 1994.

[20] P. Lalonde and A. Fournier. A Wavelet Representation of Reflectance Functions. *IEEE Transactions on Visualization and Computer Graphics*, 3(4):329–336, August 1997.

[21] Robert R. Lewis and Alain Fournier. Light-Driven Global Illumination with a Wavelet Representation. In *Rendering Techniques '96 (Proceedings of the Seventh Eurographics Workshop on Rendering)*, pages 11–20, New York, NY, 1996. Springer-Verlag/Wien.

[22] I. Daubechies. Orthonormal Bases of Compactly Supported Wavelets. *Communications on Pure and Applied Mathematics*, 41:909–996, 1988.

[23] G. Beylkin, R. Coifman, and V. Rokhlin. Fast Wavelet Transforms and Numerical Algorithms I. *Communications on Pure Applied Mathematics*, 44(2):141–183, 1991.

[24] S.G. Mallat. A Theory for Multiresolution Signal Decomposition: the Wavelet Representation. *IEEE Transactions on Part. Anal. and Mach. Int.*, 11:674–693, 1989.

[25] E. H. Adelson, E. P. Simoncelli, and R. Hingorani. Orthogonal Pyramid Transforms for Image Coding. In *Proceedings of SPIE*, volume 845, pages 50–58, 1987.

[26] Jonathan N. Bradley and Christopher M. Brislawn. The FBI Wavelet/Scalar Quantization Standard for Gray-Scale Fingerprint Image Compression. Technical Report LA-UR-93-1659, Los Alamos National Laboratory, 1993.

[27] P. P. Vaidyanathan and P.-Q. Huong. Lattice Structures for Optimal Design and Robust Implementation of Two-Channel Perfect-Reconstruction QMF Banks. *IEEE Transactions on Acoustics, Speech, and Signal Processing*, 36(1):81–94, 1988.

[28] M. Antonini, M. Barlaud, P. Mathieu, and I. Daubechies. Image Coding using Wavelet Transform. *IEEE Transactions on Image Processing*, 1:205–220, 1992.

[29] J.D. Villasenor, B. Bellzer, and B. Liao. Wavelet Filter Evaluation for Image Compression. *IEEE Transactions on Image Processing*, 4(8):1053–1060, 1995.

[30] M.J. Tsai, J. Villasenor, and F. Chen. Stack-run Image Coding. *IEEE Transactions on Circuits and Systems for Video Technology*, 6:519–521, 1996.

[31] Tilo Strutz and Erika Müller. Wavelet Filter Design For Image Compression.

[32] C. M. Brislawn. Classification of Nonexpansive Symmetric Extension Transforms for Multirate Filter Banks. *Applied and Computational Harmonic Analysis*, 3:337–357, 1996.

[33] A. Cohen, I. Daubechies, and J.C. Feauveau. Biorthogonal Bases of Compactly Supported Wavelets. *Communications on Pure and Applied Mathematics*, 45:485–560, 1992.

[34] J. Odegard and C. Burrus. Smooth Biorthogonal Wavelets for Applications in Image Compression. In *Proceedings of DSP Workshop*, 1996.

[35] Adam Finkelstein, Charles E. Jacobs, and David H. Salesin. Multiresolution Applications in Computer Graphics: Curves, Images, and Video. *Computer Graphics*, 30(Annual Conference Series):281–290, 1996.

[36] L. Claustres, M. Paulin, and Y. Boucher. BRDF Measurement Modelling using Wavelets for Efficient Path Tracing. *Computer Graphics Forum*, 22(4):701–716, 2003.

[37] W. H. Press, S. A. Teukolsky, W. T. Vetterling, and B. P. Flannery. *Numerical Recipes in C, The Art of Scientific Computing, second edition*. Cambridge University Press, Cambridge, 1992.

[38] James D. Foley, Andries van Dam, Steven K. Feiner, and John F. Hughes. *Computer Graphics, Principles and Practice, Second Edition*. Addison-Wesley, Reading, Massachusetts, 1990.

[39] David Salesin, Daniel Lischinski, and Tony DeRose. Reconstructing Illumination Functions with Selected Discontinuities. In *Third Eurographics Workshop on Rendering*, pages 99–112, Bristol, UK, May 1992.

[40] G. Serrot, M. Bodilis, X.Briottet, and H. Cosnefroy. Presentation of a new BRDF Measurement Device. *Proceeding SPIE*, 3494:34–40, 1998.

[41] L. Claustres, Y. Boucher, and M. Paulin. Spectral brdf modeling using wavelets. In *Proceedings of SPIE, Wavelet and Independent Component Analysis Applications IX, AeroSense 2002 Conference*, volume 4738, pages 33–43, 2002.

[42] Gregory J. Ward. Measuring and Modeling Anisotropic Reflection. In *Computer Graphics (ACM SIGGRAPH '92 Proceedings)*, volume 26, pages 265–272, July 1992.

[43] H. Jeffreys and B. S. Jeffreys. *The Gibbs Phenomenon in Methods of Mathematical Physics, 3rd ed.* Cambridge University Press, Cambridge, England, 1988.

[44] Robert R. Lewis. Making Shaders More Physically Plausible. In *Fourth Eurographics Workshop on Rendering*, number Series EG 93 RW, pages 47–62, Paris, France, June 1993.

[45] Y. Boucher, C. Deumié, C. Amra, L. Pinard, J.M. Mackowski, S. Mainguy, L. Hespel, and J.F. Perelgritz. Round Robin of Painted Targets BRDF Measurements. In *Proceedings of SPIE, Targets and Backgrounds VI, AeroSense 2000 Conference*, volume 4029, pages ??–??, 2000.

[46] F.A. Kruse, A.B. Lefkoff, J.B. Boardman, K.B. Heidebrecht, A.T. Shapiro, P.J. Barloon, and A.F.H. Goetz. The Spectral Image Processing System (SIPS) - Interactive Visualisation and Analysis of Imaging Spectrometer Data. *Remote Sensing of Environment*, 44:145–163, 1993.

[47] G. P. Bonneau. Optimal Triangular Haar Bases for Spherical Data. In *IEEE VIS'99 Proceedings*, 1999.

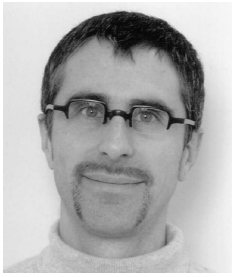
[48] R. Coifman and M. V. Wickerhauser. Entropy Based Methods for Best Basis Selection. *IEEE Transactions on Information Theory*, 38(2):719–746, 1992.

[49] S. Kaewpijit, J. Le Moigne, and T. El-Ghazawi. Spectral data reduction via wavelet decomposition. In *Proceedings of SPIE, Wavelet and Independent Component Analysis Applications IX, AeroSense 2002 Conference*, volume 4738, pages 56–63, 2002.

Brief biographies



Luc Claustres received the M.S. and Ph.D. degrees both in Computer Science from the Université Paul Sabatier (UPS), Institut de Recherche en Informatique de Toulouse (IRIT), Toulouse, France, in 2000 and 2003, respectively. He was also Assistant Professor at the UPS from 2000 to 2003. He joined the CS company in the Fall of 2003, where presently he holds the rank of Research Engineer. His areas of research interest are physically-based rendering using acquired radiometric terms, radiative transfer simulation, signal processing using wavelets and real-time character animation.



Yannick Boucher received the Engineer degree in Physics in 1988 from the Ecole Nationale Supérieure de Physique (ENSPM), Marseille, France. He entered at the Office National d'Etudes et Recherches Aérospatiales (ONERA) as a Research Scientist in 1990 for working on laser reference star for adaptive optics. He jointed the Thermo-Optics Research Unit of the Optics Department (DOTA/QDO) of the ONERA Toulouse Center in 1997. His research was then focused on the measurement and modelling of spectral and directional optical properties of targets and backgrounds. He has now the responsibility of the studies on hyperspectral imagery.



Mathias Paulin completed is Ph.D. in Computer Science at the Institut de Recherche en Informatique de Toulouse (IRIT) in Decembre 1995. In 1996, he was Assistant Professor at the Université Paul Sabatier (UPS) and became Associate Professor in 1997. He is now leading the *Visualisation and Rendering* research group at IRIT. His research interests include physically based rendering, high quality real-time rendering and advanced architecture for computer graphics.

Tables

r_c	8:1		16:1		32:1	
Case	ϵ_1^r	ϵ_2^r	ϵ_1^r	ϵ_2^r	ϵ_1^r	ϵ_2^r
r1	1.4	2	3.2	4.2	8.6	13
r2	0.68	1.2	1	1.8	2.3	4.5
l1	3.5	6.5	4.9	9.2	6.1	11
l2	9.5	16	14	22	25	32
e1	0.57	0.76	0.87	1.1	1.6	2.1
e2	0.94	1.2	1.9	2.3	4.6	5.6

Table 1: Relative modelling error (%) achieved on different measured spectra for a large set of compression ratios.

BRDF	spectralon 800nm		cloth 700nm		plastic 700nm	
r_c	ϵ_1^r	ϵ_2^r	ϵ_1^r	ϵ_2^r	ϵ_1^r	ϵ_2^r
1:1	0.014	0.06	0.054	0.27	0.091	0.65
2:1	0.091	0.15	0.53	0.77	0.24	0.7
8:1	0.52	0.65	1.4	1.9	1.1	1.6
16:1	0.85	1	2.3	3.1	9.3	14
64:1	1.6	2	3.8	5.2	54	113
128:1	1.9	2.4	4.4	6	52	113
256:1	2.8	3.3	4.9	6.8	47	113

BRDF	green grass 800nm		dry grass 600nm		sand 800nm	
r_c	ϵ_1^r	ϵ_2^r	ϵ_1^r	ϵ_2^r	ϵ_1^r	ϵ_2^r
1:1	0.081	0.4	0.065	0.29	0.089	0.41
2:1	0.53	0.79	0.26	0.46	0.28	0.53
8:1	1.5	1.8	2.1	2.6	1.1	1.4
16:1	2.1	2.7	3.1	3.7	1.7	2.2
64:1	3.3	4.2	6.2	7.6	2.7	3.3
128:1	5.2	7	9.8	12	5.6	7.7
256:1	7.3	10	10	13	6.1	8

Table 2: Relative modelling errors (%) achieved on isotropic BRDFs at fixed wavelength acquired with our goniometer.

BRDF	spectralon			plywood			cloth		
r_c	ϵ_1^r	ϵ_2^r	basis	ϵ_1^r	ϵ_2^r	basis	ϵ_1^r	ϵ_2^r	basis
1:1	0.078	0.36	-	0.26	1.2	-	0.53	2.8	-
2:1	0.18	0.41	FBI	0.43	1.3	CDF3_5	1.3	3.2	Coiflet1
8:1	0.27	0.46	Villasenor5	0.65	1.4	CDF3_5	6	10	CDF3_1
16:1	0.36	0.54	Villasenor5	0.73	1.4	CDF2_8	7.1	12	CDF3_1
64:1	0.5	0.74	Villasenor1	1.3	2.2	Villasenor2	7.4	12	Coiflet1
128:1	0.63	0.92	CDF2_2	2	3	Villasenor1	9.5	16	BurtAdelson
256:1	0.92	1.1	Villasenor1	4.4	6.3	Villasenor1	11	19	CDF2_4

BRDF	sand			plastic			wood		
r_c	ϵ_1^r	ϵ_2^r	basis	ϵ_1^r	ϵ_2^r	basis	ϵ_1^r	ϵ_2^r	basis
1:1	0.25	1	-	0.42	2.9	-	0.14	1.2	-
2:1	0.58	1.1	Villasenor6	0.75	3	Coiflet4	0.72	1.6	Daubechies3
8:1	0.71	1.2	Symmlet4	1.7	4.9	Coiflet4	0.93	1.9	Daubechies3
16:1	1.1	1.6	Symmlet6	2	5.1	Daubechies10	3.1	7.5	CDF4_4
64:1	1.6	2.2	Villasenor3	8	13	Brislawn2	4.4	9.4	Villasenor2
128:1	2.4	3	Symmlet6	8.8	20	CDF4_4	5.6	11	CDF4_4
256:1	2.8	3.5	Villasenor3	15	30	Brislawn2	7.8	12	Villasenor6

Table 3: Relative modelling errors (%) achieved on spectral isotropic BRDFs acquired with our goniometer.

(a)

BRDF	velvet		Ward	
r_c	ϵ_1^r	ϵ_2^r	ϵ_1^r	ϵ_2^r
1:1	0.05	1.2	0	0
2:1	0.059	1.5	0.32	0.076
8:1	4.8	11	3.1	5.4
16:1	7.6	15	8.5	15
32:1	9.6	62	13	22
64:1	15	227	16	28
128:1	19	236	17	30

(b)

BRDF	velvet		
r_c	ϵ_1^r	ϵ_2^r	basis
1:1	1.3	4.5	-
2:1	2.9	7.1	CDF3_5
4:1	3.1	7.7	CDF3_5
8:1	6.3	25	Villasenor18_10
16:1	12	40	Brislawn2
32:1	17	52	Villasenor1

Table 4: Relative modelling errors (%) achieved on anisotropic BRDFs acquired with our goniometer: (a) at a fixed wavelength of 650nm, (b) for a spectral range 400-950 nm.

case	I	II
ϵ_1^r (%)	1.3	2.7
ϵ_2^r (%)	1.7	4
as_1	0.017	0.037
as_2	0.017	0.037
as_3	0.017	0.037

Table 5: Initial modelling error for virtual BRDF noise free data and two different compression ratios.

level	0.2% (a)			1% (b)			5% (c)		
case	initial	I	II	initial	I	II	initial	I	II
ϵ_1^r (%)	0.25	1.8	2.7	1.2	1.9	2.8	6.2	3.2	3.4
ϵ_2^r (%)	0.28	2.5	4	1.4	2.5	4	7	4.4	4.7
as_1	0.0028	0.024	0.037	0.013	0.024	0.037	0.068	0.048	0.049
as_2	0.0029	0.024	0.037	0.013	0.024	0.037	0.069	0.024	0.037
as_3	0.0026	0.024	0.037	0.013	0.025	0.037	0.067	0.025	0.033

Table 6: Relative modelling errors and spectral angle values for virtual BRDF data with different levels of multiplicative noise.

level	$2.5 * 10^{-4}$ (d)			10^{-3} (e)			$5 * 10^{-3}$ (f)		
case	initial	I	II	initial	I	II	initial	I	II
ϵ_1^r (%)	0.76	1.4	2.8	3	2.5	3.6	15	10	10
ϵ_2^r (%)	1.3	1.9	4	5.2	4.3	5.1	26	20	18
as_1	0.0039	0.017	0.038	0.015	0.018	0.037	0.079	0.057	0.052
as_2	0.0042	0.017	0.037	0.017	0.017	0.037	0.086	0.027	0.036
as_3	0.0024	0.017	0.037	0.0096	0.016	0.035	0.048	0.016	0.033

Table 7: Relative modelling errors and spectral angle values for virtual BRDF data with different levels of additive noise.

List of figures

Figure 1: BRDF modelling process: (a) analytical approach, (b) numerical approach.

Figure 2: Hemispherical subdivision at level 0, 1, and 2 starting from a tetrahedron. Each triangle is split into four children almost equal in term of solid angles at each subdivision step.

Figure 3: Multiresolution analysis on the sphere $\mathcal{S}^2$: (a) scaling functions defined on a triangle, (b) wavelet functions defined on a triangle.

Figure 4: Compression rates achieved according to different wavelet bases, for a constant modelling error $\epsilon_2^r = 2$ %, on different acquired spectra.

Figure 5: Spectrum reconstruction of an acquired paint emissivity from different compression ratios.

Figure 6: Spectrum reconstruction of an acquired sand radiance from different compression ratios.

Figure 7: Different reconstructed BRDF compared to measurements: (a) cloth BRDF in the principal plane $\phi_i = 0°$ for $\theta_i = 60°$ (450nm), (b) sand BRDF in the principal plane $\phi_i = 0°$ for $\theta_i = 60°$ (700nm), (c) dry grass BRDF in the plane $\phi = 40°$ for $\theta_i = 50°$ (800nm).

Figure 8: Spectral isotropic BRDF of the cloth target reconstructed with two different wavelet bases and compression ratios, represented here for $\theta_i = \theta_r = 60°$, $\phi = 180°$.

Figure 9: Spectral isotropic BRDF of the spectralon panel reconstructed with two different wavelet bases and compression ratios. The compression smooths the BRDF and removes the noise ($\theta_i = \theta_r = 30°$, $\phi = 180°$).

Figure 10: Illustration of the Gibbs Phenomenon for the reconstructed velvet

BRDF. Negative values in the original BRDF are clamped to 10^{-6} ($\theta_i = 0°$, $\theta_r = 10°$, $\phi_i = \phi_r = 0°$).

Figure 11: Method of the model sensitivity to BRDF measurement noise.

Figure 12: Comparison of the different BRDF sets (noise-free uncompressed, noise-free compressed, noisy uncompressed, and noisy compressed) for a multiplicative noise level of 5% and a compression ratio of 16:1 ($\theta_i = 60°$, $\theta_r = 30°$, $\phi = 180°$).

Figure 13: Identical to previous figure but in the principal plane $\phi_i = 0°$ for $\theta_i = 60°$ (800nm).

Figure 14: Comparison of the different BRDF sets (as in Figure 12) for an additive noise level equal to $5 * 10^{-3}$ and a compression ratio of 8:1 ($\theta_i = \theta_r = 60°$, $\phi = 0°$).

Figures

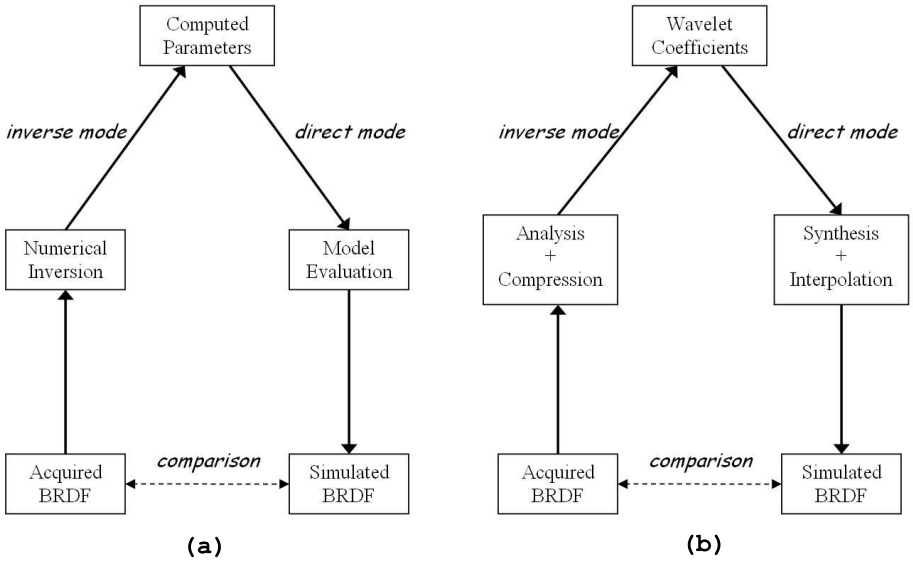


Figure 1:

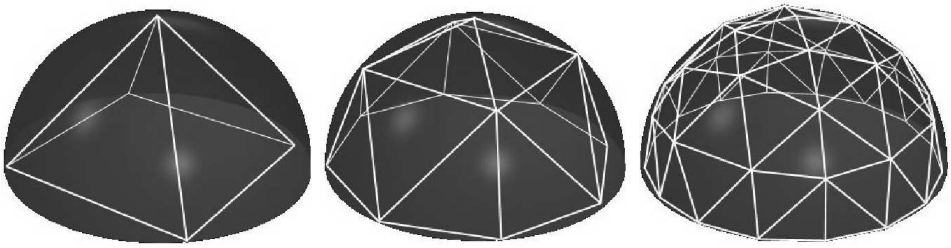
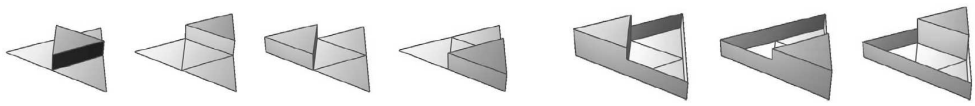


Figure 2:



(a) (b)

Figure 3:

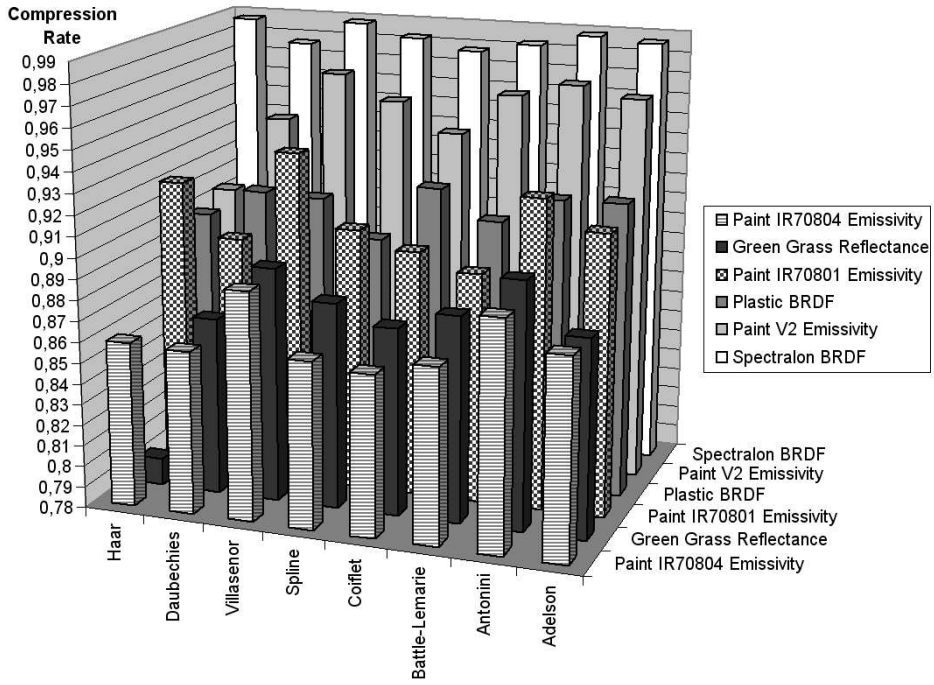

Compression Rate
0,99
0,98
0,97
0,96
0,95
0,94
0,93
0,92
0,91
0,9
0,89
0,88
0,87
0,86
0,85
0,84
0,83
0,82
0,81
0,8
0,79
0,78
Haar
Daubechies
Villasenor
Spline
Coiflet
Battle-Lemarie
Antonini
Adelson
Spectralon BRDF
Paint V2 Emissivity
Plastic BRDF
Paint IR70801 Emissivity
Green Grass Reflectance
Paint IR70804 Emissivity
Paint IR70804 Emissivity
Green Grass Reflectance
Paint IR70801 Emissivity
Plastic BRDF
Paint V2 Emissivity
Spectralon BRDF

Figure 4:

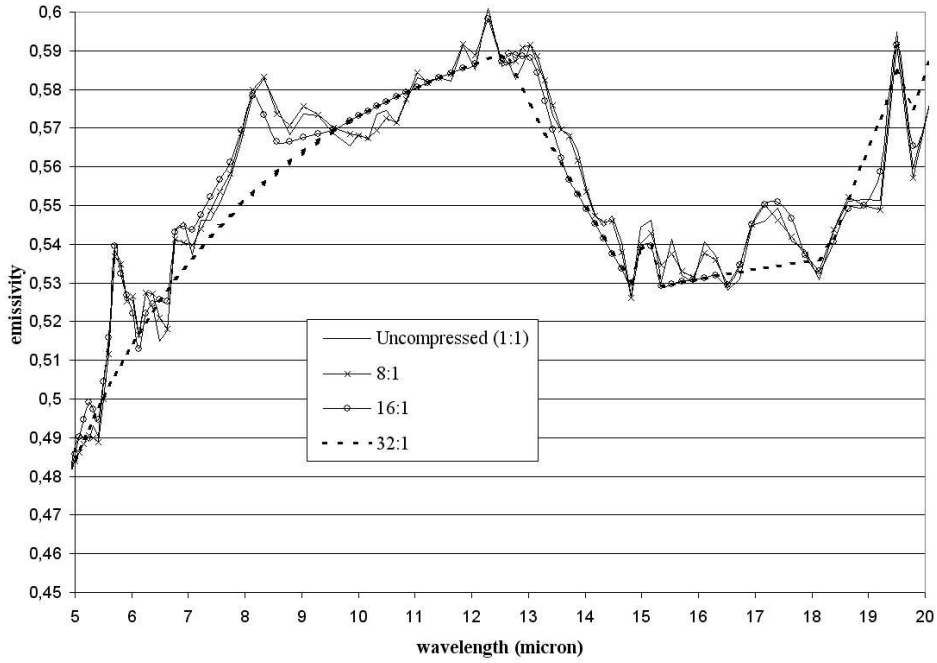

0,6
0,59
0,58
0,57
0,56
0,55
0,54
0,53
0,52
0,51
0,5
0,49
0,48
0,47
0,46
0,45
emissivity
Uncompressed (1:1)
8:1
16:1
32:1
5
6
7
8
9
10
11
12
13
14
15
16
17
18
19
20
wavelength (micron)

Figure 5:

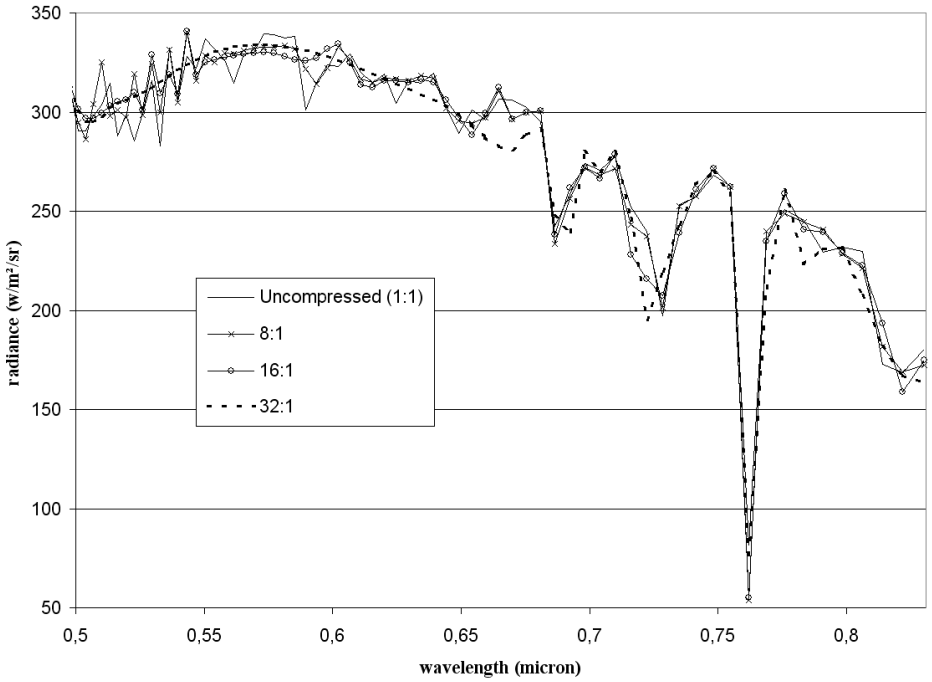
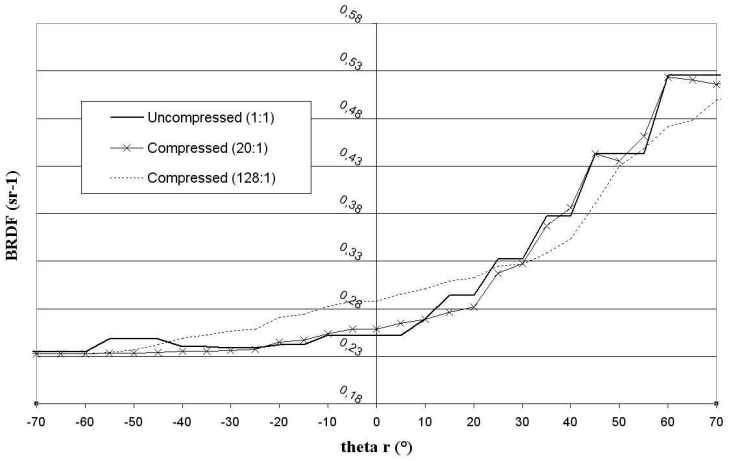
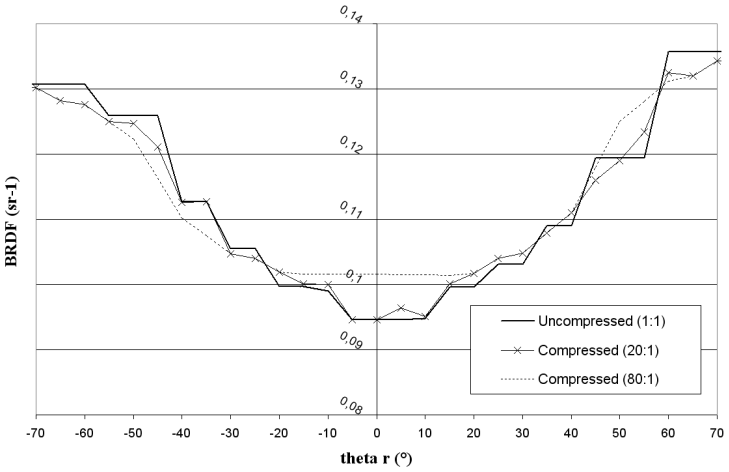

350
300
250
200
150
100
50
radiance (w/m²/sr)
0,5
0,55
0,6
0,65
0,7
0,75
0,8
wavelength (micron)
Uncompressed (1:1)
8:1
16:1
32:1

Figure 6:

(a)


Uncompressed (1:1)
Compressed (20:1)
Compressed (128:1)
BRDF (sr-1)
theta r (°)

(b)


Uncompressed (1:1)
Compressed (20:1)
Compressed (80:1)
BRDF (sr-1)
theta r (°)

(c)

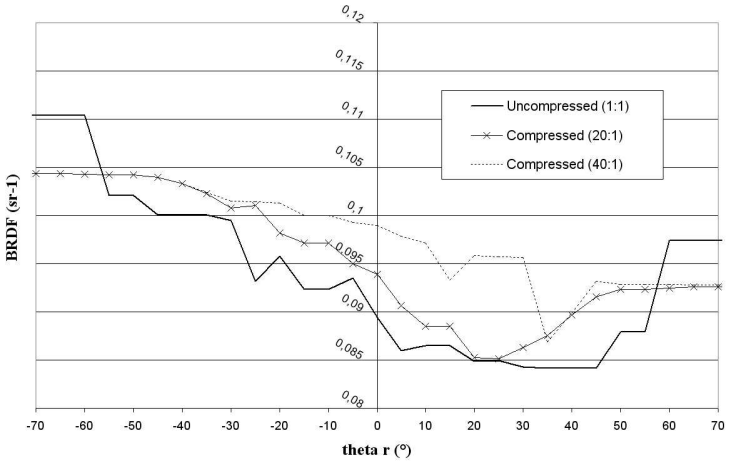

Uncompressed (1:1)
Compressed (20:1)
Compressed (40:1)
BRDF (sr-1)
theta r (°)

Figure 7:

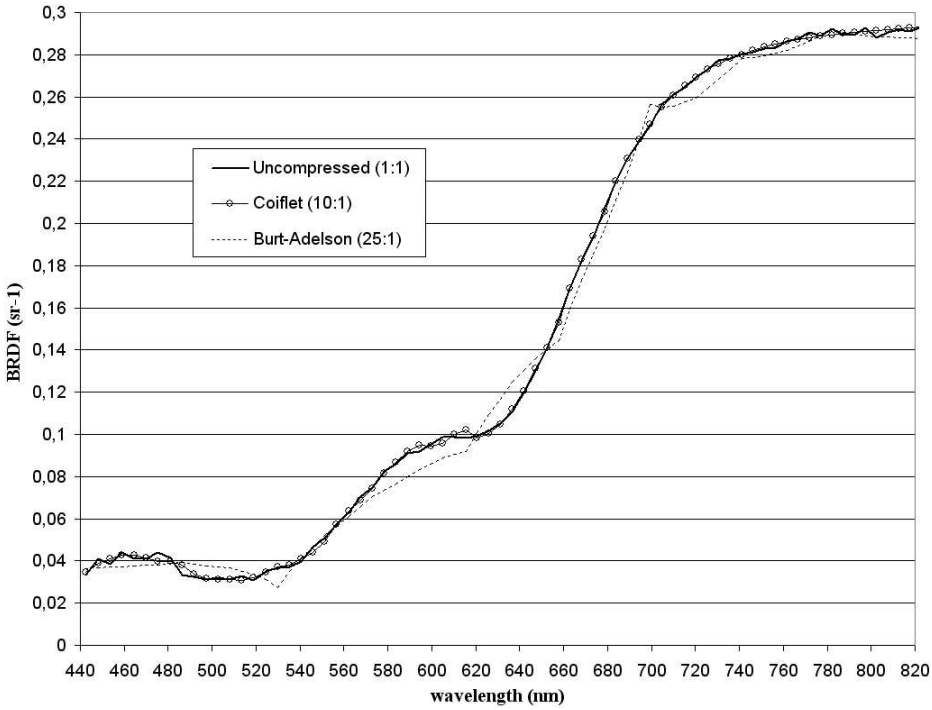

0,3
0,28
0,26
0,24
0,22
0,2
0,18
0,16
0,14
0,12
0,1
0,08
0,06
0,04
0,02
0
BRDF (sr-1)
Uncompressed (1:1)
Coiflet (10:1)
Burt-Adelson (25:1)
440 460 480 500 520 540 560 580 600 620 640 660 680 700 720 740 760 780 800 820
wavelength (nm)

Figure 8:

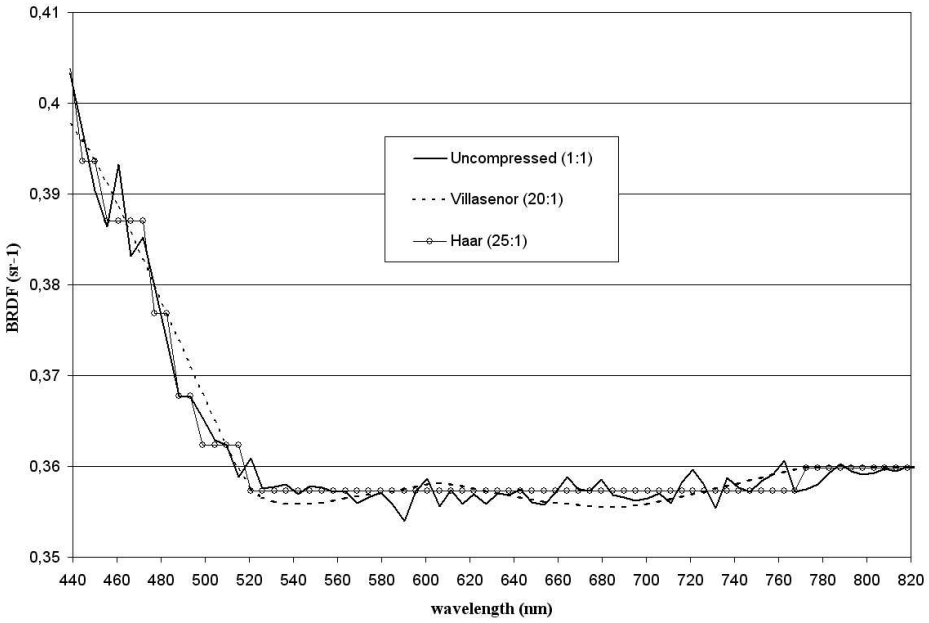

0,41
0,4
0,39
0,38
0,37
0,36
0,35
BRDF (sr-1)
Uncompressed (1:1)
Villasenor (20:1)
Haar (25:1)
440 460 480 500 520 540 560 580 600 620 640 660 680 700 720 740 760 780 800 820
wavelength (nm)

Figure 9:

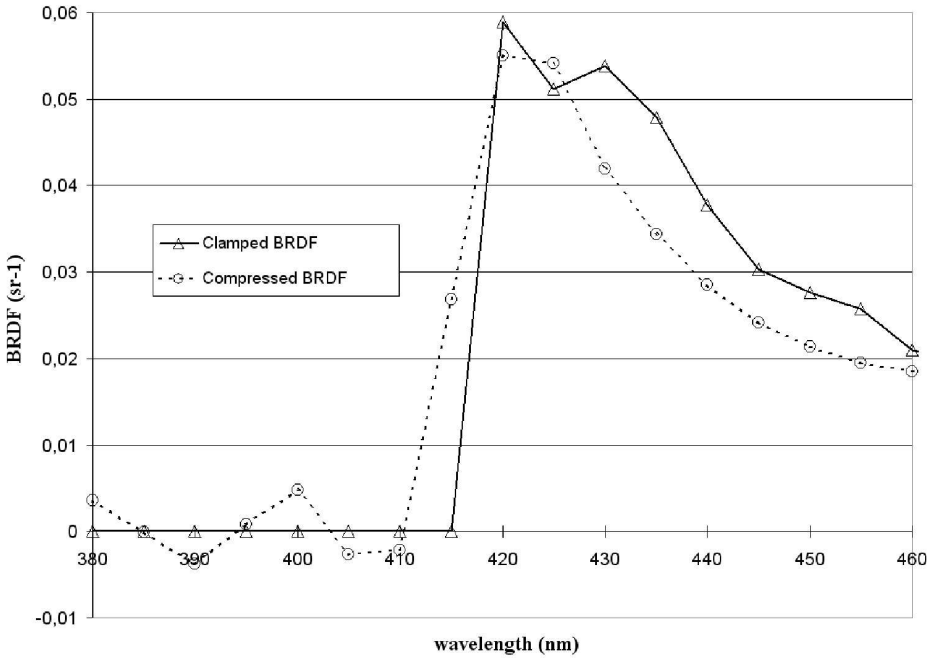

0,06
0,05
0,04
0,03
0,02
0,01
0
-0,01
BRDF (sr-1)
Clamped BRDF
Compressed BRDF
380
390
400
410
420
430
440
450
460
wavelength (nm)

Figure 10:

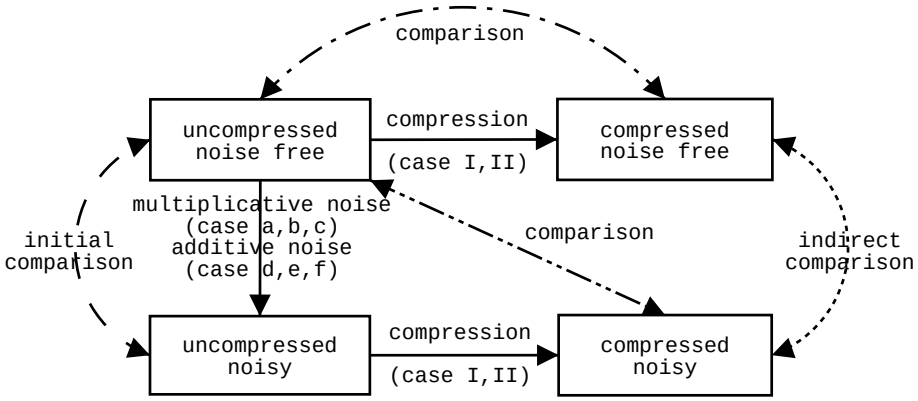

comparison
uncompressed
noise free
compression
(case I,II)
compressed
noise free
multiplicative noise
(case a,b,c)
additive noise
(case d,e,f)
initial
comparison
comparison
indirect
comparison
uncompressed
noisy
compression
(case I,II)
compressed
noisy

Figure 11:

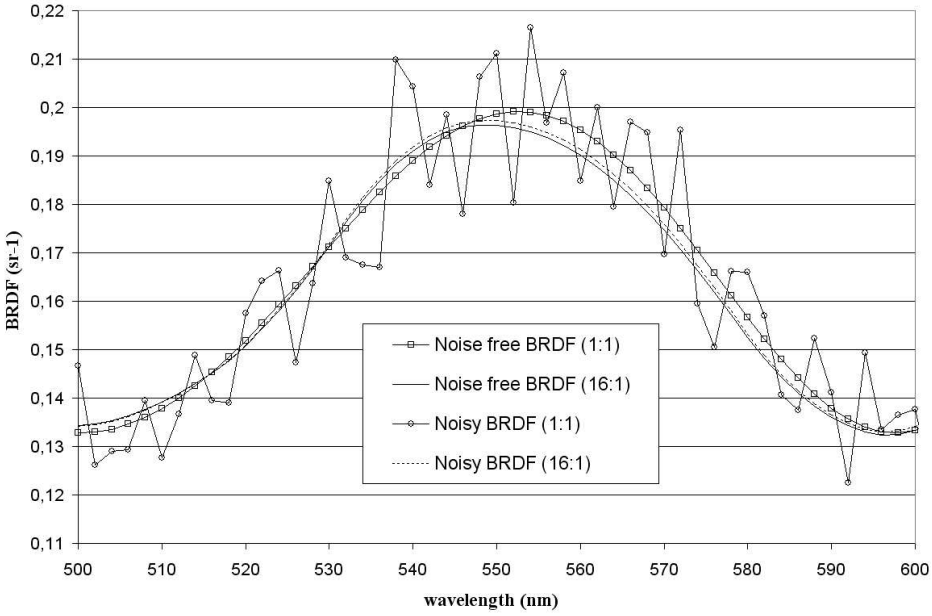

0,22
0,21
0,2
0,19
0,18
0,17
0,16
0,15
0,14
0,13
0,12
0,11
BRDF (sr-1)
500
510
520
530
540
550
560
570
580
590
600
wavelength (nm)
Noise free BRDF (1:1)
Noise free BRDF (16:1)
Noisy BRDF (1:1)
Noisy BRDF (16:1)

Figure 12:

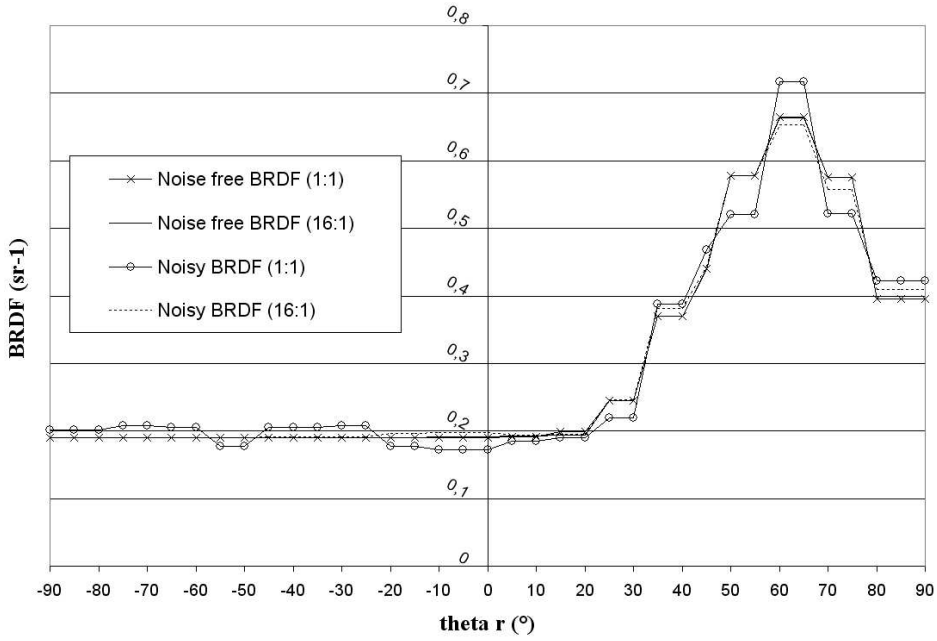

BRDF (sr-1)
0,8
0,7
0,6
0,5
0,4
0,3
0,2
0,1
0
Noise free BRDF (1:1)
Noise free BRDF (16:1)
Noisy BRDF (1:1)
Noisy BRDF (16:1)
-90 -80 -70 -60 -50 -40 -30 -20 -10 0 10 20 30 40 50 60 70 80 90
theta r (°)

Figure 13:

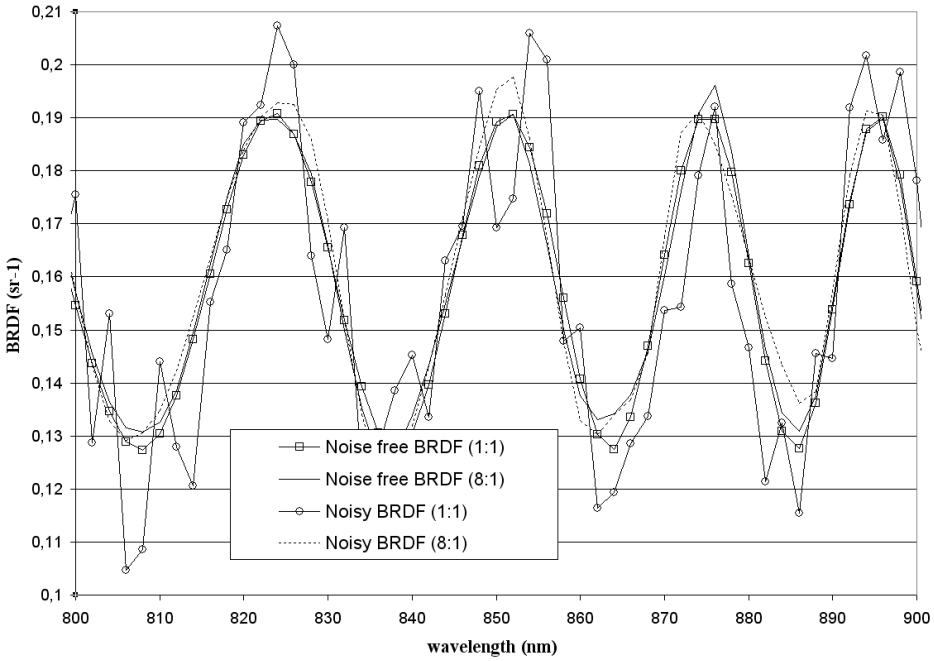

0,21
0,2
0,19
0,18
0,17
0,16
0,15
0,14
0,13
0,12
0,11
0,1
BRDF (sr-1)
800
810
820
830
840
850
860
870
880
890
900
wavelength (nm)
Noise free BRDF (1:1)
Noise free BRDF (8:1)
Noisy BRDF (1:1)
Noisy BRDF (8:1)

Figure 14: